 DOI: 10.3217/978-3-85125-954-4-02

On the Regularising Levenberg-Marquardt Method for Blinn-Phong Photometric Stereo

Georg Radow and Michael Breuß
Chair of Applied Mathematics
Brandenburg University of Technology Cottbus-Senftenberg
{radow,breuss}@b-tu.de

Abstract

Photometric stereo refers to the process to compute the 3D shape of an object using information on illumination and reflectance from several input images from the same point of view. The most often used reflectance model is the Lambertian reflectance, however this does not include specular highlights in input images. In this paper we consider the arising non-linear optimisation problem when employing Blinn-Phong reflectance for modeling specular effects. To this end we focus on the regularising Levenberg-Marquardt scheme. We show how to derive an explicit bound that gives information on the convergence reliability of the method depending on given data, and we show how to gain experimental evidence of numerical correctness of the iteration by making use of the Scherzer condition. The theoretical investigations that are at the heart of this paper are supplemented by some tests with real-world imagery.

1. Introduction

The photometric stereo (PS) problem is a fundamental task in computer vision [5]. The aim of PS is to infer the 3D shape of an object from a set of multiple images. Thereby the images depict an object from the same perspective, but the illumination direction changes throughout the images. An important information besides the illumination is the light reflectance of the object. The classic PS model [13, 14] is formulated in terms of Lambertian light reflectance. A Lambertian surface is characterised by diffuse reflectance and the independence of perceived shading from the viewing angle. The Lambertian set-up is certainly convenient for modeling, as it represents the most simple mathematical model for reflectance, and thus resulting formula and inverse problems are relatively simple. However, it is quite well known that in PS specular highlights [6] as well as non-Lambertian diffuse effects [7] may have an important impact on 3D reconstruction.

Let us also comment on some other basic characteristics of PS. Depending on the knowledge on the lighting, one discerns between calibrated and uncalibrated PS. In this work we consider only the calibrated case, where lighting directions and intensities are known. Furthermore, the final goal of PS is to obtain a depth map, such that for each relevant image pixel three-dimensional information of the depicted object is obtained. While some approaches tackle this problem directly in terms of depth values [8], the more common strategy is to divide depth computation into two sub-problems. In doing so at first a map of normal vectors is computed, from which the (relative) depth is obtained in a second step. See for instance [11] for a survey on surface normal integration. In this paper we only consider the first of the latter tasks, that is to find the normal vectors. Another aspect is sometimes the projection performed by the camera during image acquisition, often leading to orthographic or perspective models, respectively. In this work we address effectively both settings.

Our contribution. In this paper, we consider some theoretical aspects of practical value in the optimisation of PS when using Blinn-Phong reflectance. Here we extend in several ways upon previous work; let us especially refer to [6], where the Blinn-Phong model is employed in a similar way as here. Thereby, we consider to include the potentially most important specularity parameter, the so-called shininess, as an unknown in the optimisation, which is in contrast to [6] and many other works in the field. The approximate solution of the non-linear optimisation problem arising pixelwise is performed by the regularising Levenberg-Marquardt method, see especially [2]. As this is an iterative method, it is important to assess the influence of initialisation on the convergence and to give a rigorous bound as a stopping criterion. Furthermore as the problem is non-linear, one can observe in practical examples, that it may be difficult to minimise the underlying residual. To address this issue we investigate the use of a coarse-to-fine (CTF) scheme as well as an initialisation obtained through classical PS. We show how to explore Scherzer's criterion [3], which appeared in [4] for the first

time. This criterion is considered for theoretical purposes within the construction of the method, in order to assess the convergence property in our PS problem experimentally.

2. Classical Photometric Stereo

Let us reiterate the classic PS approach of Woodham [13, 14]. Given is a set of $m \geq 3$ images $(\mathcal{I}_1, \dots, \mathcal{I}_m)^\top =: \mathcal{I}$, so that $\mathcal{I} : \Omega \to \mathbb{R}^m$, along with the corresponding lighting directions $L_k \in \mathbb{R}^3$ with $\|L_k\| = 1$ for $k = 1, \dots, m$, with associated intensities $l_k \geq 0$. Throughout the paper $\|\cdot\|$ denotes the Euclidean norm or the induced spectral norm. The object to be reconstructed is depicted usually as a non-rectangular domain $\Omega \in \mathbb{R}^2$, which is embedded in the image domain.

The surface normal vectors $\mathcal{N} : \Omega \to \mathbb{R}^3$ with $\|\mathcal{N}(x,y)\| = 1$ for all $(x,y)^\top \in \mathbb{R}^2$ and the albedo $\rho^d : \Omega \to \mathbb{R}$ are fitted through a least squares approach, by minimising

$$\iint_\Omega \left\|\mathcal{R}^{\mathrm{L}}(x,y) - \mathcal{I}(x,y)\right\|^2 \mathrm{d}x\,\mathrm{d}y, \tag{1}$$

with reflectance function $\mathcal{R}^{\mathrm{L}} \coloneqq \left(\mathcal{R}^{\mathrm{L}}_1, \dots, \mathcal{R}^{\mathrm{L}}_m\right)^\top$, consisting of components

$$\mathcal{R}^{\mathrm{L}}_k \coloneqq \rho^d l_k L_k^\top \mathcal{N}, \quad k = 1, \dots, m. \tag{2}$$

In practice this boils down to finding a local solution $N \in \mathbb{R}^3$ at every sample location $(x,y)^\top$ for the problem

$$\min_N \|LN - I\|^2, \quad L \coloneqq \begin{pmatrix} l_1 L_1^\top \\ \vdots \\ l_m L_m^\top \end{pmatrix}, \quad I \coloneqq \mathcal{I}(x,y). \tag{3}$$

This, in turn, leads to the computation of the normal vectors and, as a byproduct, the albedo according to

$$N = \left(L^\top L\right)^{-1} L^\top I, \tag{4}$$

$$\rho^d(x,y) = \|N\|, \qquad \mathcal{N}(x,y) = N/\|N\|\,. \tag{5}$$

3. Blinn-Phong Photometric Stereo

In the general least squares approach Eq. (1), we can modify the reflectance function to account for non-Lambertian effects. To this end we investigate the Blinn-Phong (BP) model [1, 9], which has the form $\mathcal{R}^{\mathrm{BP}} \coloneqq \left(\mathcal{R}^{\mathrm{BP}}_1, \dots, \mathcal{R}^{\mathrm{BP}}_m\right)^\top$ with components

$$\mathcal{R}^{\mathrm{BP}}_k \coloneqq \rho^d l_k L_k^\top \mathcal{N} + \rho^s h_k \max\left\{0, \mathcal{H}_k^\top \mathcal{N}\right\}^\alpha, \tag{6}$$

$k = 1, \dots, m$. We observe by (6) that in the BP model, diffuse reflection as in (2) is supplemented by a specular reflection term. Here $\rho^s : \Omega \to \mathbb{R}$ denotes the specular albedo. Another material parameter is the specular sharpness or shininess $\alpha : \Omega \to \mathbb{R}$. The halfway vectors $\mathcal{H}_k : \Omega \to \mathbb{R}^3$ depend on the viewing directions $\mathcal{V} : \Omega \to \mathbb{R}^3$ and are computed for $k = 1, \dots, m$ as

$$\mathcal{H}_k(x,y) \coloneqq H_k/\|H_k\|, \qquad H_k \coloneqq L_k + \mathcal{V}(x,y). \tag{7}$$

Making use of focal length f, the viewing directions $\mathcal{V}^\perp$ and $\mathcal{V}^\angle$ in the orthographic and perspective setting respectively are

$$\mathcal{V}^\perp = (0,0,1)^\top, \qquad \mathcal{V}^\angle(x,y) = (x,y,f)^\top. \tag{8}$$

We reinterpret l_k as diffuse intensity of the light source and denote $h_k \geq 0$ as specular intensity. To ensure that image intensities are only increased due to diffuse and specular terms, it is reasonable to enforce $\rho_d, \rho_s \geq 0$. Furthermore $\rho_d, \rho_s \leq 1$ ensures that at most as much image intensity is added as light intensity is supplied by each light source. Finally, it is reasonable to enforce $\alpha > 1$ to actually produce specular highlights through the specular term.

The BP model was originally proposed for computer graphics. It is not based on physical laws, but it enables to create plausible images with a still simple model compared to other possible approaches. Despite its simplicity, for use in inverse problems in computer vision, the non-linearities in Eq. (6) may pose considerable hurdles.

Let us now discuss the modeling of the components in Eq. (6) along with a few adaptations we employ. First we turn our attention to the normal vectors $\mathcal{N}$. One may model them through derivatives of the depth or its logarithm. In this approach we may parametrise them at a specific location through depth derivatives p, q as

$$\mathcal{N}(x,y) = \frac{N(p,q)}{\|N(p,q)\|}. \tag{9}$$

However the step of obtaining a normal vector of length 1 in Eq. (9) adds another layer of non-linearity to the model. In numerical experiments we found this approach to be not very reliable. Therefore we opt for an approach in analogy to classical PS. In Eq. (6) we replace $\rho^d \mathcal{N} = N$ introducing the auxiliary variable $r = \rho^s/(\rho^d)^\alpha$.By furthermore replacing $\alpha = 1 + \exp(a)$ we ensure that $\mathcal{R}^{\mathrm{BP}}$ has continuous first derivatives. Eq. (6) then takes the form

$$\mathcal{R}^{\mathrm{BP}}_k(N, r, a) = l_k L_k^\top N + r h_k \max\left\{0, \mathcal{H}_k^\top N\right\}^{1+\exp(a)}, \tag{10}$$

with $r, a \in \mathbb{R}$ and $N \in \mathbb{R}^3$.

4. On the Optimisation Strategy

With BP reflectance, we have to solve a non-linear least squares problem, to which end we utilise the regularising Levenberg-Marquardt (RLM) scheme [2, 3]. Writing the

underlying task in standard notation, with this algorithm one may aim to find a solution $\vec{x}$ of the problem

$$F(\vec{x}) = \vec{y}, \qquad F : \mathbb{R}^n \to \mathbb{R}^m, \tag{11}$$

with a known differentiable function F. Let us note that the description and discussion of the RLM algorithm in [3] is in a more general setting. For simplicity we only give an overview of the algorithm based on finite dimensional spaces, as is fitting for the problem at hand.

It is furthermore assumed that the original data $\vec{y}$ is not known, but with some $\delta > 0$ an estimate is required on how good the given data $\vec{y}^\delta$ approximates the original data, according to

$$\left\|\vec{y}^\delta - \vec{y}\right\| \leq \delta. \tag{12}$$

Then with some starting point $\vec{x}_0$ the iterative rule takes the form

$$\vec{x}_{k+1} = \vec{x}_k + \left(F'(\vec{x}_k)^\top F'(\vec{x}_k) + \alpha_k I_n\right)^{-1} F'(\vec{x}_k)^\top \left(\vec{y}^\delta - F(\vec{x})\right) \tag{13}$$

with Jacobian matrix F', $n \times n$-dimensional identity matrix I_n and a regularisation weight $\alpha_k > 0$ such that with a preassigned $\rho \in (0, 1)$ the new iterate $\vec{x}_{k+1}$ fulfils

$$\left\|\vec{y}^\delta - F(\vec{x}_k) - F'(\vec{x}_k)\left(\vec{x}_{k+1} - \vec{x}_k\right)\right\| = \rho\left\|\vec{y}^\delta - F(\vec{x}_k)\right\|. \tag{14}$$

The *stopping criterion* of the RLM scheme depends explicitly on the noise level δ in the given data. To stop at an iterate $\vec{x}_k$, it has to fulfil

$$\left\|\vec{y}^\delta - F(\vec{x}_k)\right\| \leq \tau\delta, \tag{15}$$

with a preassigned $\tau > 2$, fulfilling $\rho\tau > 1$. For numerical experiments we set $\rho = 0.5,\ \tau = 2.5$, following [3].

The discussion of the RLM scheme in [3] relies on the strong Scherzer condition [4]. For the Jacobian matrices at two points $\vec{x}_1, \vec{x}_2 \in \mathbb{R}^n$ there exists a matrix $R = R(\vec{x}_1, \vec{x}_2)$ such that $F'(\vec{x}_1) = RF'(\vec{x}_2)$ and

$$\|R - I_m\| \leq C^R \|\vec{x}_1 - \vec{x}_2\| \tag{16}$$

with some $C^R > 0$, which is constant for all $\vec{x}_1, \vec{x}_2 \in \mathbb{R}^n$. This condition imposes a certain regularity of the Jacobian matrix F'. In this context we are interested in a local approximation of C^R. For two consecutive iterations $\vec{x}_k, \vec{x}_{k+1}$ we estimate R as a solution of $F'(\vec{x}_k) = R(\vec{x}_k, \vec{x}_{k+1})F'(\vec{x}_{k+1})$ with minimal norm. Then we can locally approximate the constant in Eq. (16) as

$$C_k^{R,\text{loc}} = \frac{\|R(\vec{x}_k, \vec{x}_{k+1}) - I_m\|}{\|\vec{x}_k - \vec{x}_{k+1}\|}. \tag{17}$$

Since F in Eq. (11) is nonlinear, we employ a CTF framework. In doing so the data is scaled to a coarser scale, *i.e.* to a lower resolution. The obtained result is then used as initialisation on the next finer scale, until we arrive at the original resolution.

Let us focus on the assumption Eq. (12). The noise level δ governs the stopping criterion of the RLM scheme. If Eq. (12) is not fulfilled then the iterates may actually diverge.

At this point we make the assumption that our data $\mathcal{I}(x, y)$ is a realisation of the BP model corrupted by additive white Gaussian noise, *i.e.* it can be modelled as

$$\mathcal{I}(x, y) = \mathcal{R}(x, y) + \varepsilon(x, y), \quad \text{for } (x, y)^\top \in \Omega. \tag{18}$$

Here $\varepsilon(x, y)$ is a realisation of a multivariate normal distribution, such that the m components are independent and identically distributed (i.i.d.) with mean zero and standard deviation $\sigma > 0$, the corresponding density function is

$$f(X) = \frac{1}{\sqrt{2\pi}^m \sigma^m} \exp\left(-\frac{1}{2\sigma^2}\sum_{i=1}^m X_i^2\right), \tag{19}$$

cf. [10]. The probability that Eq. (12) holds can be computed with the following result. The proof, which is technical but straightforward, is included for the readers convenience. The following result is also related to the Chi distribution.

Proposition 1. *Let $m \in \mathbb{N}$, $\delta > 0$ and let ε be a realisation of an m-dimensional multivariate normal distribution with mean zero, standard deviation $\sigma > 0$ and density Eq.* (19)*. The probability of $P \coloneqq P(\|\varepsilon\| \leq \delta|\sigma, m)$ can be computed as follows:*

(i) If m is even, then

$$P = 1 - \exp\left(-\frac{\delta^2}{2\sigma^2}\right) \sum_{i=0}^{\frac{m}{2}-1} \left(\frac{\delta^2}{2\sigma^2}\right)^i \frac{1}{i!}. \tag{20}$$

(ii) If m is odd, then

$$P = \sqrt{\frac{2}{\pi}}\left(\frac{1}{\sigma}\int_0^\delta \exp\left(-\frac{r^2}{2\sigma^2}\right)\mathrm{d}r - \exp\left(-\frac{\delta^2}{2\sigma^2}\right) \sum_{i=1}^{\frac{m-1}{2}} \left(\left(\frac{\delta}{\sigma}\right)^{m-2i} \prod_{j=1}^{\frac{m+1}{2}-i}\left(\frac{1}{2j-1}\right)\right)\right). \tag{21}$$

Proof. For any continuous probability density f we have

$$P = P(\|\varepsilon\| \leq \delta|\sigma, m) = \int_{\|X\|\leq\delta} f(X)\,\mathrm{d}X. \tag{22}$$

Since the density function in Eq. (19) is radially symmetric, this simplifies to

$$P = \int_0^\delta O_m(r) f(r, 0, \ldots, 0)\,\mathrm{d}r, \tag{23}$$

where

$$O_m(r) = 2r^{m-1}\frac{\pi^{\frac{m}{2}}}{\Gamma\left(\frac{m}{2}\right)} \tag{24}$$

denotes the surface area of a sphere with radius r around the origin in $\mathbb{R}^m$. Γ denotes the gamma function. Inserting Eq. (19), we write

$$P = \frac{2^{1-\frac{m}{2}}}{\sigma^m\Gamma\left(\frac{m}{2}\right)}\int_0^\delta r^{m-1}\exp\left(-\frac{r^2}{2\sigma^2}\right)\mathrm{d}r. \tag{25}$$

Since $\int r\exp(r^2/(2a))\,\mathrm{d}r = a\exp(r^2/(2a)) + c$, for $m > 2$ the integral in Eq. (25) can be simplified by partial integration, *i.e.*

$$\begin{aligned}\int_0^\delta r^{m-2}\cdot r\exp\left(-\frac{r^2}{2\sigma^2}\right)\mathrm{d}r \\ = -\sigma^2\left[r^{m-2}\exp\left(-\frac{r^2}{2\sigma^2}\right)\right]_{r=0}^{\delta} \\ + \sigma^2(m-2)\int_0^\delta r^{m-4}\cdot r\exp\left(-\frac{r^2}{2\sigma^2}\right)\mathrm{d}r.\end{aligned} \tag{26}$$

We now consider the two cases of m being even or odd.

Let $m \in \mathbb{N}$ be even. Then repeated partial integration of the integral Eq. (25) leads to

$$\begin{aligned}&\int_0^\delta r^{m-1}\exp\left(-\frac{r^2}{2\sigma^2}\right)\mathrm{d}r \\ &= -\sum_{i=1}^{\frac{m}{2}-1}\sigma^{2i}\prod_{j=1}^{i-1}(m-2j)\left[r^{m-2i}\exp\left(-\frac{r^2}{2\sigma^2}\right)\right]_{r=0}^{\delta} \\ &\quad + \sigma^{m-2}\prod_{j=1}^{\frac{m}{2}-1}(m-2j)\int_0^\delta r\exp\left(-\frac{r^2}{2\sigma^2}\right)\mathrm{d}r \\ &= -\sum_{i=1}^{\frac{m}{2}}\sigma^{2i}\prod_{j=1}^{i-1}(m-2j)\left[r^{m-2i}\exp\left(-\frac{r^2}{2\sigma^2}\right)\right]_{r=0}^{\delta} \\ &= -\sum_{i=1}^{\frac{m}{2}}\sigma^{2i}\frac{2^{i-1}\left(\frac{m}{2}-1\right)!}{\left(\frac{m}{2}-i\right)!}\left[r^{m-2i}\exp\left(-\frac{r^2}{2\sigma^2}\right)\right]_{r=0}^{\delta} \\ &= \sigma^m 2^{\frac{m}{2}-1}\left(\frac{m}{2}-1\right)! \\ &\quad -\sum_{i=1}^{\frac{m}{2}}\sigma^{2i}\frac{2^{i-1}\left(\frac{m}{2}-1\right)!}{\left(\frac{m}{2}-i\right)!}\delta^{m-2i}\exp\left(-\frac{\delta^2}{2\sigma^2}\right).\end{aligned} \tag{27}$$

This formula can easily be verified for $m = 2$, as in this case the initial integral simplifies to the form $\int r\exp(r^2/(2a))\,\mathrm{d}r$. Inserting Eq. (27) and $\Gamma(m/2) = (m/2-1)!$ into Eq. (25), we obtain after an index shift Eq. (20).

Now let $m \in \mathbb{N}$ be odd. Again we use repeated partial integration on the integral in Eq. (25), until we arrive at

$$\begin{aligned}&\int_0^\delta r^{m-1}\exp\left(-\frac{r^2}{2\sigma^2}\right)\mathrm{d}r \\ &= \sigma^{m-1}\prod_{j=1}^{\frac{m-1}{2}}(2j-1)\int_0^\delta\exp\left(-\frac{r^2}{2\sigma^2}\right)\mathrm{d}r \\ &\quad -\sum_{i=1}^{\frac{m-1}{2}}\sigma^{2i}\frac{\prod_{j=1}^{\frac{m-1}{2}}(2j-1)}{\prod_{j=1}^{\frac{m+1}{2}-i}(2j-1)}\delta^{m-2i}\exp\left(-\frac{\delta^2}{2\sigma^2}\right).\end{aligned} \tag{28}$$

Plugging this together with

$$\begin{aligned}\Gamma\left(\frac{m}{2}\right) = \Gamma\left(\frac{m-1}{2}+\frac{1}{2}\right) = \frac{(m-1)!\sqrt{\pi}}{\left(\frac{m-1}{2}\right)!\,2^{m-1}} \\ = \frac{\prod_{j=1}^{\frac{m-1}{2}}((2j)(2j-1))\sqrt{\pi}}{2^{\frac{m-1}{2}}\prod_{j=1}^{\frac{m-1}{2}}(2j)} = \frac{\sqrt{\pi}}{2^{\frac{m-1}{2}}}\prod_{j=1}^{\frac{m-1}{2}}(2j-1)\end{aligned} \tag{29}$$

into Eq. (25) leads to Eq. (21). □

5. Experiments

Since we focus on the computed vector fields of surface normals, it appears adequate to employ colour coding of surface normals for visual assessment, *cf.* Figure 1. For quantitative evaluation we consider here the standard AAE, where the averaging is performed over the object domain. Let us note that we use the result obtained through classical PS as an initialisation for the BP model. Throughout the experiments we computed δ according to Proposition 1, such that Eq. (12) is fulfilled with a probability of 95%. We observed that the choice of this confidence level is not critical for the outcome of our experiments.

Synthetic Test Example. As a synthetic experiment for our investigations we consider the *sphere* example, see Figure 1. Let us note that we consider an orthographic setting for all the *sphere* experiments. As we observe in Figure 1, in this experiment the developed computational model and set-up enables to obtain a nearly perfect result. For optimisation we employed in total 5 input images, of which we show here just one example. For comparison, we give here the corresponding result obtained by Lambertian PS applied at analogous input images where we filtered the specular highlights by the subspace technique proposed in [15], which is supposed to make the input nearly Lambertian. As is confirmed here visually as well as quantitatively, it appears favorable (at least in this example) to explore an explicit modeling like with the proposed BP framework.

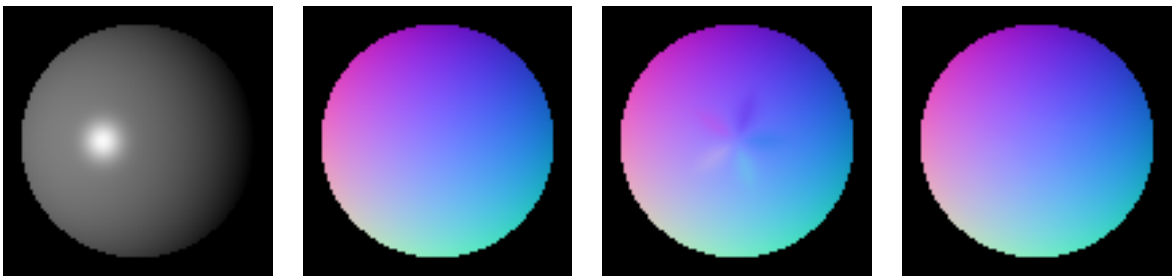

Figure 1. *(left-to-right:)* one of the input images of the *sphere* rendered using the BP model; colour coded vector field of ground truth normal vectors; classical PS with preprocessing [15], average angular error (AAE) 1.02; developed BP framework with CTF, AAE 0.37

Let us note that in fact this test example may not be too easy, as can be observed by the results obtained by preprocessing and Lambertian PS. The reason is that the specular highlights in the input are not perfectly distributed over the sphere and may result in distortions if not being accounted for sufficiently accurate in the model.

Evaluation of Scherzer's Condition. As discussed in Sec. 4, between two iterates of the RLM scheme we observe the local approximation $C_k^{R,\mathrm{loc}}$ of the constant in Eq. (16) according to Eq. (17). As the Scherzer condition is an important assumption for the results in [3], we opt to add a break condition, where the algorithm stop if the estimate grows too large. In practice the algorithm is halted if we observe an iterate with $C_k^{R,\mathrm{loc}} \geq 2000$. As can be seen in Figs. 2 and 3 this is usually the case at locations where specular highlights may occur, as the angle between halfway vectors and surface normals becomes small. One may interprete this result in the way, that the energy that is minimised features at highlights many small variations that makes it difficult to obtain a reliable local minimum.

We evaluated the restarting of the RLM scheme with a larger parameter ρ in Eq. (14), if it stopped before an iterate fulfils Eq. (15). This may lead to a smaller trust region and to a more stable behaviour of the algorithm. However we did in general not observe a significant increase in quality. The results displayed here were thus computed without restarting the RLM scheme, giving an account of the unstabilised version of the method.

Real World Test Example. In order to assess the properties and usefulness of the developed numerical BP framework, we exploit here a selected variety of examples taken from the *DiLiGent* data set [12] which gives an account of photographed real-world objects with different reflectance properties. Here we do not employ a CTF scheme, as we rely on the initialisation obtained with classical PS. Let us note that the underlying model is now (in practice, weakly) perspective.

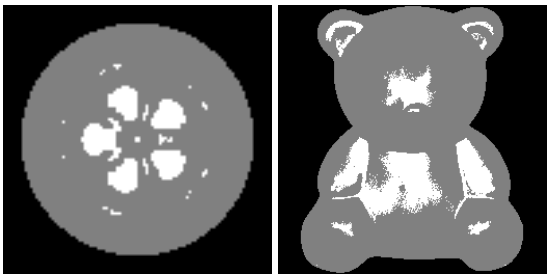

Figure 2. Algorithmic behaviour in the *sphere* experiment *(left)* and an example from the *DiLiGent* data set [12] *(right)*. White depicts the locations where the RLM scheme stopped due to the $C_k^{R,\mathrm{loc}} \geq 2000$ criterion.

As can be visually assessed by means of Figure 3, the proposed model along with its adaptations performs very reasonably but in some details not perfect, depending on the actual example. For clarifying thereby the zones of influence of the specular terms we depict masks showing the object parts where the BP model gives an effective contribution. When taking into account the properties of the considered examples, it appears especially that the broad specularities as appearing in the input (teddy bear, goblet) may result in a certain inaccuracy. In turn, when highlights appear but are not too strong (cat, tea pot), results are quite convincing, given that the underlying reflectance in these cases is supposed to be non-linear in the diffuse reflectance as the underlying material is rough. In the tested real world setting from *DiLiGent* the results are overall of similar quality to the preprocessed Lambertian method. Therefore we conjecture that our numerical BP framework appears to be especially suited for dealing with objects with not too strong highlights, being at the same time able to tackle a certain range of diffuse reflectance of rough materials.

6. Conclusion

We discussed the BP reflectance in the context of PS. The augmentation of classical PS with this reflectance model is

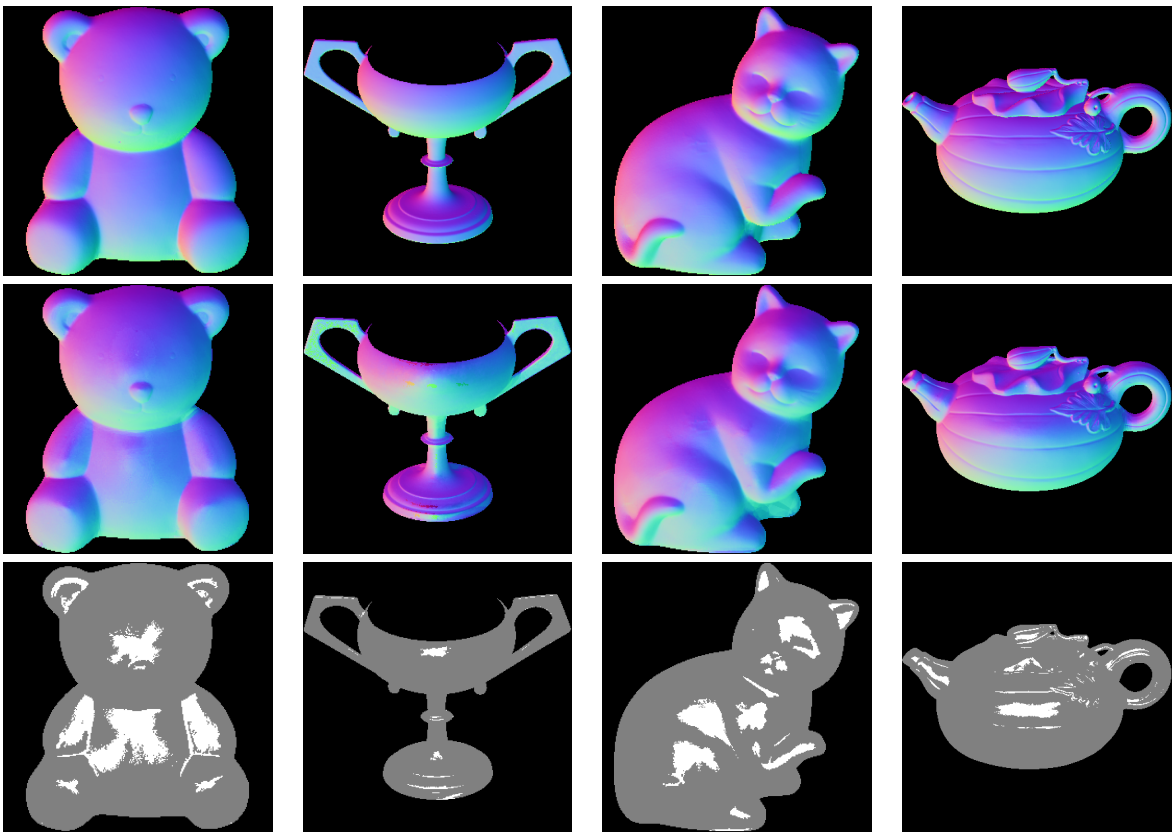

Figure 3. *(left-to-right:)* Examples from *Diligent* data sets. *(top-to-bottom:)* Visualisation of ground truth normals; normal fields based on BP (where we note the effect of the not satisfied Scherzer condition at some highlights at the goblet); mask based on half directions. White depicts locations where the maximum of the cosines between halfway vectors and the normal vector obtained with classical PS is ≥ 0.99.

straightforward, but solving the arising optimisation problem is less so. This task can be tackled with the RLM scheme, which leads to satisfactory results.

The findings for the implementation of the RLM scheme may be translated to other problems, since the assumption that the data follows a normal distribution is very common. The application of the BP model to more complex data sets poses considerable hurdles, which may be adressed in future work.

References

[1] J. F. Blinn. Models of light reflection for computer synthesized pictures. In *Proceedings of the 4th annual conference on Computer graphics and interactive techniques - SIGGRAPH '77*. ACM Press, 1977.

[2] M. Hanke. A regularizing Levenberg - Marquardt scheme, with applications to inverse groundwater filtration problems. *Inverse Problems*, 13(1):79–95, 1997.

[3] M. Hanke. The regularizing Levenberg-Marquardt scheme is of optimal order. *Journal of Integral Equations and Applications*, 22(2):259–283, 2010.

[4] M. Hanke, A. Neubauer, and O. Scherzer. A convergence analysis of the Landweber iteration for nonlinear ill-posed problems. *Numerische Mathematik*, 72(1):21–37, 1995.

[5] B. K. P. Horn. *Robot Vision*. MIT Electrical Engineering and Computer Science. MIT Press, 1986.

[6] M. Khanian, A. S. Boroujerdi, and M. Breuß. Photometric stereo for strong specular highlights. *Computational Visual Media*, 4(1):83–102, 2018.

[7] G. McGunnigle, J. Dong, and X. Wang. Photometric stereo applied to diffuse surfaces that violate lambert's law. *Journal of the Optical Society of America A*, 29(4):627, mar 2012.

[8] R. Mecca, A. Tankus, A. Wetzler, and A. M. Bruckstein. A direct differential approach to photometric stereo with perspective viewing. *SIAM Journal on Imaging Sciences*, 7(2):579–612, 2014.

[9] B. T. Phong. Illumination for computer generated pictures. *Communications of the ACM*, 18(6):311–317, 1975.

[10] S. J. D. Prince. *Computer Vision: Models, Learning, and Inference*. Cambridge University Press, 2012.

[11] Y. Quéau, J.-D. Durou, and J.-F. Aujol. Normal integration: A survey. *Journal of Mathematical Imaging and Vision*, 60(4):576–593, 2017.

[12] B. Shi, Z. Mo, Z. Wu, D. Duan, S. K. Yeung, and P. Tan. A benchmark dataset and evaluation for non-Lambertian and uncalibrated photometric stereo. *IEEE Transactions on Pattern Analysis and Machine Intelligence*, pages 1–14, 2018.

[13] R. J. Woodham. Photometric stereo: A reflectance map technique for determining surface orientation from image intensity. In Ramakant Nevatiam, editor, *Image Understanding Systems and Industrial Applications*, volume 155 of *Proceedings of the Society of Photo-Optical Instrumentation Engineers*, pages 136–143. SPIE, 1978.

[14] R. J. Woodham. Photometric method for determining surface orientation from multiple images. *Optical Engineering*, 19(1):134–144, 1980.

[15] L. Wu, A. Ganesh, B. Shi, Y. Matsushita, Y. Wang, and Y. Ma. Robust photometric stereo via low-rank matrix completion and recovery. In *Asian Conference on Computer Vision (ACCV)*, volume 6494 of *Lecture Notes in Computer Science*, pages 703–717. Springer Berlin Heidelberg, 2010.